Snapshot three-dimensional absorption imaging of microscopic specimens

Yongjin Sung*
College of Engineering & Applied Science, University of Wisconsin, Milwaukee, WI 53211, USA
(Dated: May 17, 2021)

Snapshot projection optical tomography (SPOT) uses a micro-lens array (MLA) to simultaneously capture the projection images of a three-dimensional (3D) specimen corresponding to different viewing directions. Compared to other light-field imaging techniques using an MLA, SPOT is dual telecentric and can block high-angle stray rays without sacrificing the light collection efficiency. Using SPOT, we recently demonstrated snapshot 3D fluorescence imaging. Here we demonstrate snapshot 3D absorption imaging of microscopic specimens. For the illumination, we focus the incoherent light from a light-emitting diode onto a pinhole, which is placed at a conjugate plane to the sample plane. SPOT allows us to capture the ray bundles passing through the specimen along different directions. The images recorded by an array of lenslets can be related to the projections of 3D absorption coefficient along the viewing directions of lenslets. Using a tomographic reconstruction algorithm, we obtain the 3D map of absorption coefficient. We apply the developed system to different types of samples, which demonstrates the optical sectioning capability. The transverse and axial resolutions measured with gold nanoparticles are 1.3 μm and 2.3 μm, respectively.

I. INTRODUCTION

The absorption by a specimen has served as an imaging contrast since the beginning of optical imaging. In tandem with various spectroscopic techniques, the absorption imaging can provide the molecular fingerprint as well as the structural information. For a thick specimen, three-dimensional (3D) imaging is required, as two-dimensional (2D) imaging can observe only a thin slice of the volume. The depth of field of a high-resolution bright-field microscope is only a couple of micrometers[1]. For 3D imaging, a series of 2D thin slices is typically acquired while changing the imaging focus, then a deconvolution is applied to the acquired stack of images[2]. Alternatively, the 3D internal structure of a specimen can be reconstructed from a series of images recorded for varying angles of illumination[3]. The intensity in each image can be related to a projection (i.e., integral along the beam propagation direction) of the 3D absorption coefficient. The so-called projection images are typically acquired in sequence, because the incident angle of the illumination beam needs be changed in each step as is done in X-ray computed tomography (CT)[4].

For a microscopic specimen, a variety of methods have been proposed to record the projection images in a single snapshot[5–9]. Most notably, light-field microscopy (LFM) records the 4D light field, i.e., the magnitude and direction of each ray bundle that forms an image, using a micro-lens array (MLA) placed at the image plane[10]. The projection images can be synthesized from the recorded 4D light field after deconvolution. The second class of LFM places the MLA at the pupil plane or the back focal plane of objective lens, which allows recording the projection images directly[11–14]. In our previous work[15], we have shown a third class of LFM, which places the MLA in a 4F telecentric configuration with the objective lens and installs an aperture stop at the back focal plane of a relay lens. This technique we named as Snapshot projection optical tomography (SPOT) is dual telecentric and can block high-angle stray rays without sacrificing the light collection efficiency. SPOT was originally demonstrated for 3D fluorescence imaging, which is extended here to 3D absorption imaging. For the original SPOT system, any conventional illuminator capable of fluorescence excitation can be used. For the new system, the existing illuminator for bright-field imaging is not optimal; therefore, we designed our own illuminator for trans-illumination. Existing LFMs have also been demonstrated for transmission imaging[10, 11, 13]. We note, however, that the demonstrated axial resolution was far worse than the transverse resolution, which is possibly due to the recording of a small number of projection images, the use of a small angular range of the illumination beam, or both. Here we introduce a design that can generate the beams illuminating only the field of view and having sufficiently high incidence angles with respect to the optical axis. Together with SPOT, it allows for 3D absorption imaging of a microscopic specimen in a single snapshot.

II. THEORY

Figure 1 shows schematic diagrams of the illumination module and the SPOT system separately. In Fig. 1(a), the incoherent light from the light source (LS) is focused onto the pinhole (P) using the lens L1. The light after the pinhole, which consists of many beams propagating along different directions, is delivered to the sample plane (SP) by two lenses L2 and CL. The condenser lens has a high numerical aperture (NA) and small focal length compared to the lens L2. The pinhole image is projected onto the sample plane after demagnification, while the angular range of the beams after the pinhole is magni-

* yongjin.sung@gmail.com

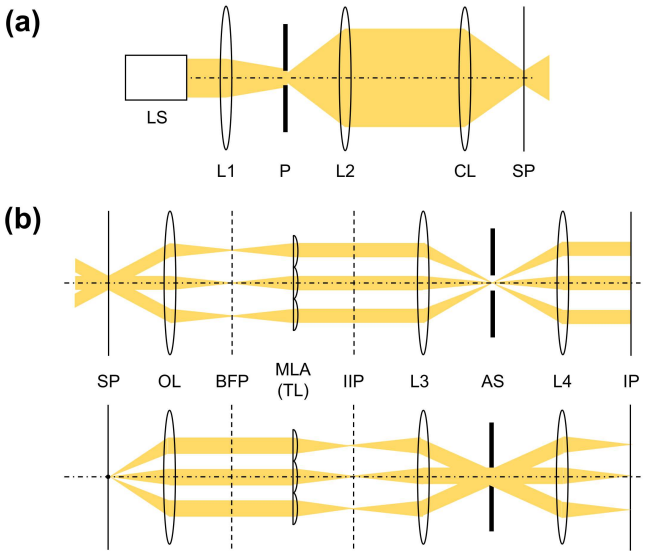

FIG. 1. Schematic diagram of SPOT for transmission imaging. (a) Illumination module and example beam path, (b) imaging module and example beam paths. In figure (b), the beam paths are traced assuming three plane waves are incident onto the sample plane from different directions (top), or three diverging beams are emitted from a point at the sample plane (bottom). LS: light source (LED); P: pinhole; L1-L4: lenses; CL: condenser lens; OL: objective lens; TL: tube lens; MLA: micro-lens array; AS: aperture stop; SP: sample plane; BFP: back focal plane of the objective lens; IIP: intermediate image plane; IP: image plane where the camera is located.

fied at the sample plane. The incoherent light incident onto the sample plane can be decomposed into infinitely many plane waves. In Fig. 1(b), we show three exemplary plane waves that pass through the sample along different directions and propagate through various optical elements in SPOT. The objective lens (OL) magnifies the beams and distributes them to the lenslets in the MLA. The two lenses L3 and L4 relay the image formed at the intermediate image plane (IIP) to the image plane (IP) with a proper magnification to achieve the Nyquist sampling rate, i.e., the sampling rate of camera is at least twice higher than the diffraction limit. An iris diaphragm between L3 and L4 serves as the aperture stop (AS), as is shown in the bottom of Fig. 1(b). The incident angles of the plane waves at the sample plane were chosen to have the beams arrive at the image plane (IP) at normal incidence. The images formed for the plane wave inputs are coherent images that we would record with a laser. As the LED light consists of infinitely many beams propagating along different directions, each lenslet captures a bundle of rays, instead of one ray, which contributes to the image generated by the lenslet. Those images are incoherent images, or to be more accurate, partially-coherent images. For example, the image formed by the on-axis lenslet is a typical bright-field image. The only difference is that the imaging resolution is determined by the NA of lenslet, not the NA of objective lens. The other images formed by the off-axis lenslets are tilted bright-field images, the ones we would get with the existing bright-field microscope if we rotated the illumination module around the center of sample plane.

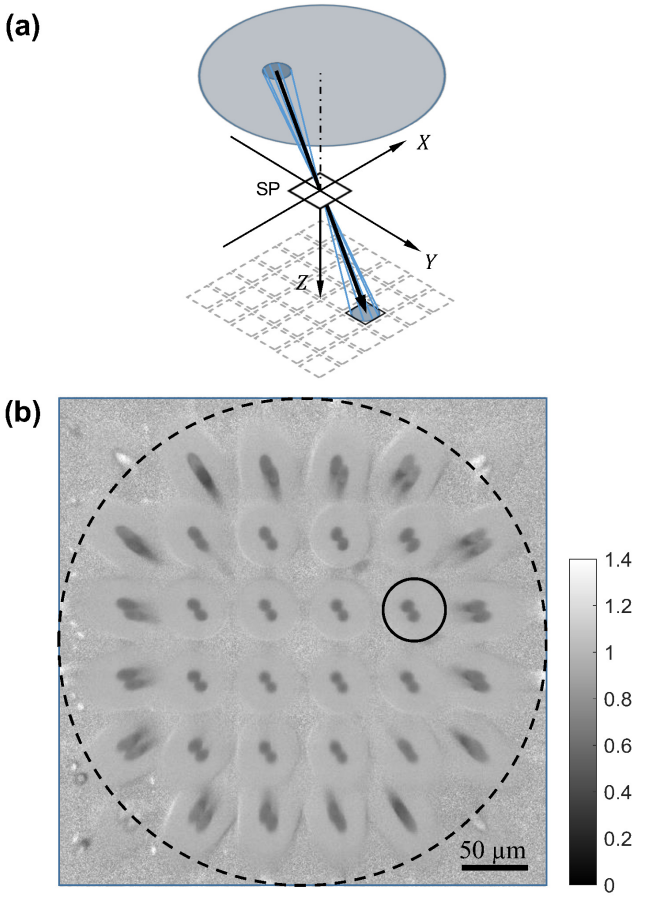

FIG. 2. Image formation (a) and example raw image (b). In figure (a), a bundle of rays, which is captured by a lenslet in the array, is traced from the condenser aperture (big circle on the top) to the lenslet aperture (solid rectangle on the bottom) through the sample plane (SP). The arrow represents the viewing angle or the projection direction for the image recorded by the lenslet. In figure (b), an example raw image is shown, after the background normalization, for two blue-dyed polystyrene beads. The dashed circle represents the objective lens aperture, and the small solid circle represents the projection image corresponding to the viewing angle shown in figure (a).

The image formation by an off-axis lenslet is further illustrated in Fig. 2(a). The big circle on the top represents the aperture of the condenser lens, while the rectangles on the bottom represent the apertures of the lenslets in the MLA. Using the illumination system in Fig. 1(a), we generate uniform light distribution in the condenser aperture, which may be considered as a collection of point light sources. Each point source generates a plane wave incident onto the sample plane (SP) from a different direction. The propagation direction of each plane wave

can be represented by a wave vector[16]. The figure shows a cone of wave vectors for the plane waves that are captured by one of the lenslets shown as a solid rectangle. The circular cross section is due to the aperture stop installed after the lens L3 in Fig. 1(b). These rays captured by the lenslet originate from the small disk in the condenser aperture. The arrow from the center of the disk to the center of the SP can be considered as the viewing direction for the projection image recorded by the lenslet. All the light rays within the cone contribute to the image recorded by the lenslet, as with bright-field microscopy. Figure 2(b) shows an example raw image obtained with the developed system. The intensity was normalized with the background image, which was recorded with an empty field of view. This background image can be acquired only once before the experiment, then used for the normalization of the sample images (i.e., the images containing the samples of interest) acquired afterward. The current design records 32 projection images with the maximum viewing angle of 43.6° with respect to the optical axis of objective lens. The dashed circle represents the aperture of the objective lens. One of the projection images is shown in the small solid circle, which corresponds to the viewing angle for the lenslet whose aperture is shown as a solid rectangle in Fig. 2(a).

For a fluorescent specimen consisting of many incoherent emitters, we previously showed that the image captured by each lenslet in SPOT can be related to the projection of the fluorophore distribution along a certain viewing direction[15]. The viewing direction is determined by the focal length of objective lens and the amount of offset of the lenslet center from the optical axis of objective lens. For transmission imaging, the recorded image is related to the projection of absorption coefficient along the viewing direction as we show below. For the 3D Cartesian coordinates (X, Y, Z), we can define the scattering potential $F(X, Y, Z)$ of a sample as $F(X, Y, Z) = -(2\pi/\lambda_0)^2[n(X, Y, Z)^2 - {n_m}^2]$, where λ_0 is the wavelength in vacuum, $n(X, Y, Z)$ is the complex-valued refractive index distribution, n_m is the refractive index of the transparent medium in which the sample is immersed[17]. Now we express $n(X, Y, Z)$ as $n_m + \Delta n(X, Y, Z)$. Assuming the refractive index increment $\Delta n(X, Y, Z)$ is small compared to n_m, we can write the scattering potential as $F(X, Y, Z) \approx -(2\pi/\lambda_0)^2 2n_m \Delta n(X, Y, Z)$. The complex-valued refractive index can be decomposed to the real (n_r) and imaginary (n_i) parts. The imaginary part is called the absorption constant and related to the attenuation coefficient by $n_i = (\lambda_0/4\pi)\,\mu_a$, where the subscript a indicates the attenuation is solely due to the absorption. Then, the scattering potential can be written as

$$F(X, Y, Z) \approx -\frac{8\pi^2}{{\lambda_0}^2} n_m \Delta n_r - i\frac{2\pi}{\lambda_0} n_m \mu_a. \tag{1}$$

Suppose that a plane wave is incident onto the sample along the direction that can be represented by a wave vector (u_0, v_0, w_0), as is shown in Fig. 3(a).

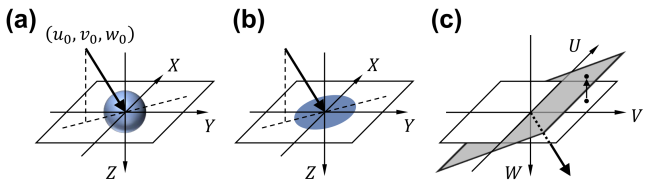

FIG. 3. Illustration of projection and back-projection operations. The 3D absorption coefficient for the sample in (a) is integrated along the direction of arrow, which represents the viewing direction, to generate the projection image in (b). This operation can be inverted by back-projecting the image in the spatial-frequency space, as is shown in (c). (X,Y,Z) represent the sample coordinates, and (U,V,W) represent the spatial-frequency coordinates, corresponding to (X,Y,Z), respectively.

Here, $\lambda_m = \lambda_0/n_m$ is the wavelength in the immersion medium, and $w_0 = \sqrt{(1/\lambda_m)^2 - {u_0}^2 - {v_0}^2}$. The scalar wave theory provides a simple relationship between the light field after the sample $U(X, Y)$ and the scattering potential $F(X, Y, Z)$[18]. With the first-order Rytov approximation[19], which is accurate for the specimens with small refractive index increment[20],

$$U(X, Y) = U_0(X, Y)\exp\{U_S(X, Y)\}, \tag{2a}$$

$$\hat{U_S}(U, V) = \frac{1}{i4\pi w}\hat{F}(U, V, W), \tag{2b}$$

where $U_0(X, Y)$ is the incident light field, U_S is the scattered field normalized with the incident field. $\hat{U_S}$ and $\hat{F}$ represent the 2D and 3D Fourier transforms of U_S and F, respectively. (U, V) are the spatial frequency coordinates corresponding to (X, Y), respectively. w and W are given by $w = \sqrt{(1/\lambda_m)^2 - u^2 - v^2}$ and $W = w - w_0$. From Eq. (2a), the intensity relationship similar to the Beer-Lambert law[21] can be derived as

$$\log\{I(X, Y)/I_0\} = 2\mathrm{Re}\{U_S(X, Y)\}, \tag{3}$$

where log is the natural logarithm.

We adopt the projection approximation, which assumes that the incident light propagates through the sample along the same initial direction. For the normal incidence, i.e., $(u_0, v_0, w_0) = (0, 0, 1/\lambda_m)$, this would produce the Beer-Lambert law. The imaging geometry adopted in this work has the incident beams with varying directions onto the sample plane, as is shown in Fig. 3(b). Note that (U, V, W) in Eq. (2) are the collection of points on a sphere with the radius of $1/\lambda_m$. Using the projection approximation, W is approximated by the following relationship.

$$W = -\frac{u_0}{w_0}U - \frac{v_0}{w_0}V. \tag{4}$$

This means the $\hat{F}$ values in Eq. (2b) are not obtained from the hemispherical surface but from the plane that

is tangent to the surface at the origin of the coordinates, which is shown in Fig. 3(c). Further, in Eq. (2b), we approximate $1/w$ as $1/w_0$. The validity of this approximation is checked later in this paper. With these approximations, the 2D inverse Fourier transform of Eq. (2) can be written as

$$U_S(X,Y) = \iiint F\left(\bar{X},\bar{Y},\bar{Z}\right) \delta\left(\bar{X} - X - \frac{u_0}{w_0}\bar{Z}, \bar{Y} - Y - \frac{v_0}{w_0}\bar{Z}\right) d\bar{X}\, d\bar{Y}\, d\bar{Z} \quad (5)$$

For each choice of (X, Y), the right hand side provides the projection, or the integral, of $F(\bar{X},\bar{Y},\bar{Z})$ along the line given by $\bar{X} + (u_0/w_0)\bar{Z} = X, \bar{Y} + (u_0/w_0)\bar{Z} = Y$.

Note that the projection direction is determined by the focal length of objective lens and the amount of offset of the lenslet center from the optical axis of objective lens. Consider the (m, n)th lenslet, whose center is located at (mp, np), where $m, n = -2.5, -1.5, -0.5, 0.5, 1.5, 2.5$, and p is the lenslet pitch. In the current notation, the projection direction (u_0, v_0, w_0) for the lenslet is given by

$$u_0 = mp/\lambda_m f_1, \quad (6a)$$

$$v_0 = np/\lambda_m f_1, \quad (6b)$$

$$w_0 = \left[{f_1}^2 - (mp)^2 - (np)^2\right]^{1/2}/\lambda_m f_1. \quad (6c)$$

We represent the projection operation along this direction as $P_{m,n}$. Substituting Eq. (1) into Eq. (5) and using Eq. (3), the intensity relationship for the image captured by the off-axis lenslet can be written as

$$\log\{I(X,Y)/I_0\} = -\frac{1}{w_0\lambda_m} P_{m,n}\{\mu_a\} \quad (7)$$

III. MATERIALS AND METHODS

Blue-dyed polystyrene microspheres were purchased from Polysciences, Inc. (18138-2). A 10 μL liquid drop of suspension (4.55×10^7 beads/mL) was mixed with distilled water at 1:30 (vol/vol) ratio. A 10 μL liquid drop from the diluted suspension was spread on a microscope slide (1 mm thickness) and covered with a No. 1 coverslip. The coverslip was fixed to the microscope slide with a tape. The sunflower pollen slide used for the demonstration was purchased from Vision Scientific Company. Gold nanoparticles of 100-nm diameter were purchased from nanoComposix, Inc. To resuspend the settled nanoparticles, the bottle containing the colloid was vigorously shaken for about 30 seconds. A 10 μL liquid drop of suspension was spread on a microscope slide (1 mm thickness) and covered with a No. 1 coverslip. The coverslip was fixed to the microscope slide with a tape.

The imaging chain of the new system uses a similar design to the original SPOT system for fluorescence imaging[15]. The field of view (i.e., the maximum sample size) and the imaging resolution have been changed slightly to incorporate the trans-illumination module with minimally increasing the system footprint. For the light source (LS), we used a high-power, white-light light-emitting-diode (LED) (Thorlabs, SOLIS-1C) with the typical output power of 4.2 W. The light output from a liquid light guide with the core diameter of 3 mm was collimated and focused onto a pinhole (600 μm diameter) using a lens with the numerical aperture (NA) of 0.6. The light from the pinhole was refocused onto the sample plane through the lens L2 (f = 100 mm) and an oil-immersion condenser lens (Nikon, 1.3 NA). After the sample, each beam was magnified with the objective lens (Nikon, Plan Apo VC 60X, 1.4 NA) and the micro-lens array (MLA). The MLA (RPC Photonics, S600-f28) had the pitch of 600 μm and the focal length of 16.8 mm. To place the MLA with a short focal length in a 4F configuration with the objective lens, we inserted two relay lenses between the objective lens and MLA, which also increased the beam size by a factor of 2.5. After the MLA, two relay lenses (L3 and L4) were used to install an iris diaphragm at the back focal plane of L3 and magnify the beams by a factor of 2.5. The iris diaphragm serves as an aperture stop (AS) for all the projection images. The raw image was recorded with a scientific complementary metal–oxide–semiconductor (sCMOS) camera (PCO, pco.edge 5.5). The overall magnification was 31.5, the field of view 48 μm, and the depth of field 8.6 μm. The diffraction limit was 1.1 μm for the wavelength of 500 nm, and the camera pixel resolution was 0.21 μm.

For data processing, the raw image was divided with a background image, which was recorded for an empty field of view, to produce the transmittance images for varying angles of incidence. Then, the logarithm of the transmittance was given as an input to the tomographic reconstruction algorithm. The reconstruction consists of two steps: deconvolution and inverse projection. For the deconvolution, we used the Richardson-Lucy method[22, 23], which is implemented as a built-in function in MATLAB (Mathworks, 2020a). In our method, the 2D deconvolution is used to simply enhance the resolution in each projection image, which contrasts with the 3D deconvolution used in other light-field microscopy techniques[10, 12, 14]. The inverse projection operation is similar to the inverse Radon transform; however, the former assumes a stationary image plane, while the latter assumes an image plane rotating around the sample[4]. To account for the stationary image plane, the inverse Radon transform was modified, as is shown in Fig. 3. The arrows in the figures represent the viewing direction for the projection image, which is calculated from the focal length of the objective lens and the offset of the lenslet center from the optical axis. For the sample shown in Fig. 3(a), the lenslet whose viewing direction is represented by the arrow records the projection image shown in Fig. 3(b). For the inverse projection, the Fourier transform of the processed image (i.e., the loga-

rithm of the transmittance) is projected onto the plane that is orthogonal to the viewing direction, as is shown in Fig. 3(c). The projection images corresponding to different viewing directions are mapped onto different planes. After completing the mapping, the 3D inverse Fourier transform provides the 3D absorption map of the imaged specimen. The tomographic reconstruction is an ill-posed inverse problem due to the small number of projection images and the finite angular range of viewing direction. The uncollected or missing data generates artefacts in the reconstructed tomogram such as the elongation along the optical axis direction and the underestimation of absorption values including negative absorption. To alleviate the ill-posedness, we applied the positivity constraint, which enforces the negative absorption to be zero, in an iterative process[24, 25]. In particular, the positivity constraint is applied to the reconstructed tomogram. The 3D Fourier transform of the modified tomogram shows the previously empty region filled with new data. This new data generated with the positivity constraint is combined with the original, unmodified data in the 3D Fourier space. Taking the 3D inverse Fourier transform, we can obtain an improved tomogram with less artefact. This process is repeated until the relative changes in pixel values are below a certain threshold. The positivity constraint used in the tomographic reconstruction improves the effective axial resolution by suppressing the missing-angle artefact.

IV. RESULTS AND DISCUSSION

First, we applied the developed system to take the 3D image of a blue-dyed polystyrene microsphere with the nominal diameter of 10 μm. Figure 4(a) shows the horizontal cross sections of the reconstructed 3D map of attenuation coefficient at 3 μm spacing. The bead cross sections are smaller at Z = $\pm$3 μm and indistinguishable at $Z = \pm 6$ μm. As with bright-field imaging, the intensity at $Z = \pm 6$ μm is not completely zero due to the residual missing-angle artefact. Nonetheless, the optical sectioning capability of the developed system is clearly shown. The attenuation coefficient measured from the center cross section ($Z = 0$) is 34.0 $\pm$ 0.9 mm^{-1} ($n = 3$). Using a broadband light source, this attenuation coefficient is the value weighted over the source spectrum. For a spectroscopic measurement, we need to add a wavelength-scanning light source or a hyperspectral camera to the system. The attenuation coefficient for the blue-dyed beads is comparable to the value we obtained with a different system using a wavelength-scanning coherent light source[26].

Next, we obtained the 3D image of a sunflower pollen grain using the developed system. Figure 4(b) shows the horizontal cross section of the reconstructed 3D map of attenuation coefficient at 4 μm spacing. The attenuation cross section clearly distinguishes the core and the surrounding envelope. We note that the first-order Rytov approximation is valid for the sample with small refractive index increment. The attenuation coefficient of blue-dyed beads was measured as $34mm^{-1}$. For the wavelength of 500 nm, this corresponds to $n_i = 0.0014$, which is negligibly small compared to the refractive index n_r of the bead (about 1.6). The pollen grain has similarly low refractive index increment. If the refractive index increment of the sample is large, the reconstruction algorithm based on the first-order Rytov approximation will provide a distorted shape and an incorrect absorption coefficient. For strongly-absorbing specimens, a more rigorous, albeit computationally expensive, reconstruction algorithm can be used[27].

Last, we measured the 3D point spread function of the developed system using gold nanoparticles (GNPs) with the nominal diameter of 100 nm. As the size of the particles is far below the resolution, it was not possible to resolve individual particles. Still, we occasionally found small dots, possibly cluttered nanoparticles, with high enough absorption contrast to be imaged with the developed system. The GNP has a large attenuation coefficient but has small diameter. To predict the scattered field from defocused GNPs, the Born approximation would be better than the Rytov approximation, although the Mie solution would be best to account for the large scattering coefficient as well as strong absorption[17]. For the GNPs at the focal plane, the simple projection approximation (ignoring the scattering) can be used. When ignoring the scattering ($w_0 \approx 1/\lambda_m$), Eq. (7) derived with the Rytov approximation is reduced to the Beer-Lambert law. From the reconstructed 3D map, we obtained the horizontal (XY) and vertical (XZ) cross sections including the pixel with the highest value, which are shown in Figs. 5(a) and 5(b), respectively. After the normalization, the center profiles (i.e., the values along the dotted lines) were fitted with Gaussian curves, as is shown in Figs. 5(c) and 5(d). The full width at half maximum (FWHM) values were used as measures of the transverse and axial resolution. The measured resolution was 1.3 μm (transverse) and 2.3 μm (axial). The magnification from the sample plane to the intermediate image plane (the back focal plane of MLA) is 12.6. The NA of 0.018 for a single lenslet corresponds to the NA of 0.23 at the sample plane. The measured resolution (1.3 μm) is slightly worse than but matches with the diffraction limit (1.1 μm) calculated for the wavelength of 500 nm. The difference may be attributed to the finite size of the cluttered nanoparticles.

For 3D absorption imaging, we added an illumination module to the existing SPOT system. The illumination module focuses the incoherent light from an LED onto a pinhole, which is located at a conjugate plane to the sample plane. Without the pinhole, the incoherent light floods the entire sample plane, and the images recorded by the lenslets are not true projections of the sample's absorption. Figure 6(a) shows the raw image acquired without the illumination pinhole and the aperture stop in the imaging beam path. The image shows a multitude

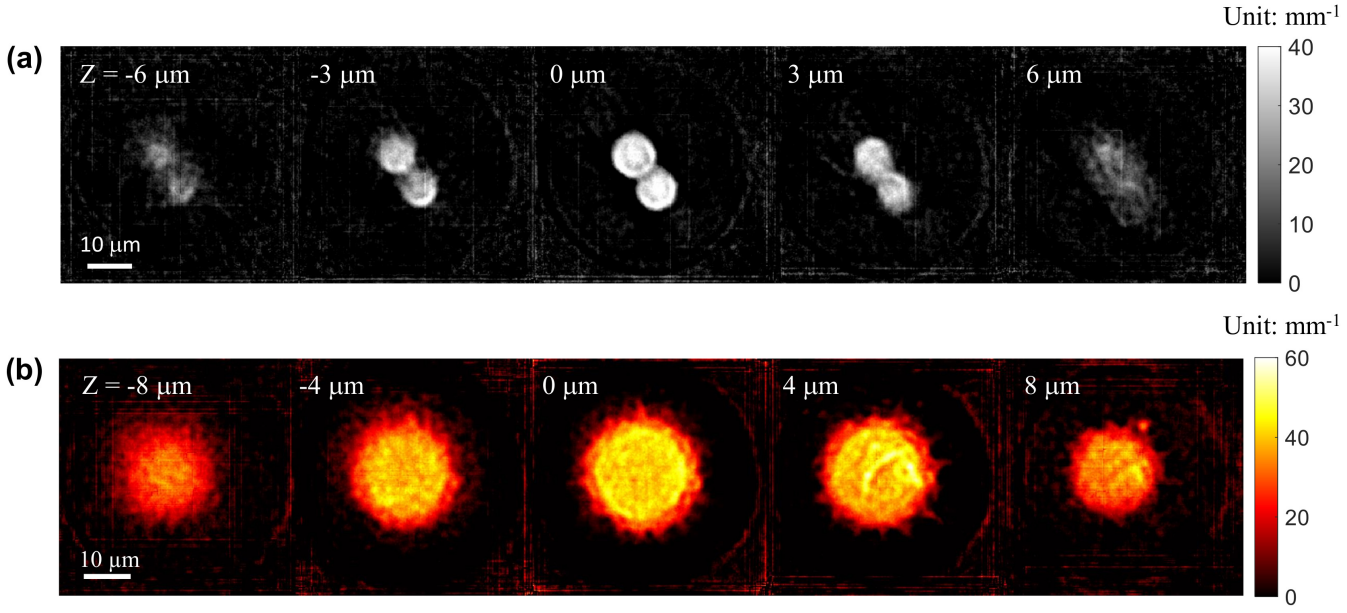

FIG. 4. Horizontal cross sections of absorption coefficient imaged with the proposed method. (a) Horizontal cross sections of two blue-dyed polystyrene beads are shown at the spacing of 3 μm. (b) Horizontal cross sections of a sunflower pollen grain are shown at the spacing of 4 μm.

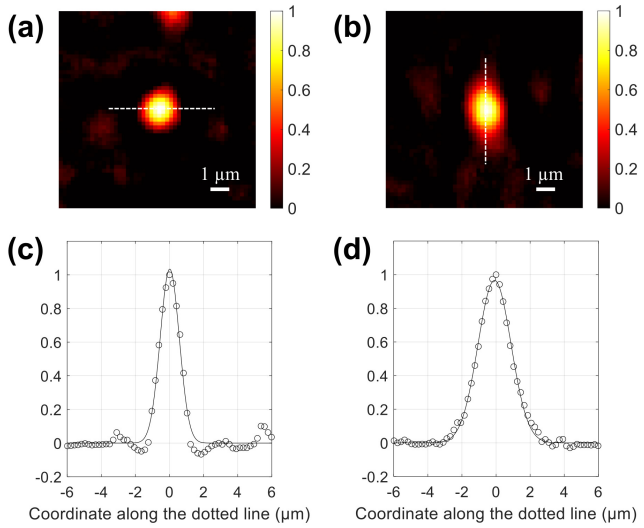

FIG. 5. 3D point spread function measurement using a gold nanoparticle. The horizontal (a) and vertical (b) cross sections of a gold nanoparticle and the profile along the dotted lines (c,d). The FWHMs of the fitted curves, which may be considered as the transverse and axial resolutions, are 1.3 μm and 2.3 μm, respectively.

of defocused lenslet boundaries, which overlap with each other. Figure 6(d) shows the same image after the normalization with a background image, the image without the sample. With the background normalization, the image is cleaner without the lenslet boundaries; however, some projection images contain ghost images of nearby beads. More important, the intensity inside the bead region is higher than expectation (i.e., the bead absorption is measured to be lower). This is possibly due to the coupling of high-angle rays from the empty surroundings into the lenslets. Figure 6(b) shows the raw image acquired without the illumination pinhole but with the aperture stop in the imaging beam path. Figure 6(e), the image after the background normalization, shows that the ghost images are completely suppressed. However, the intensity of the beads is still higher than expected, especially for the projection images close to the center. This is again attributed to coupling of high-angle rays from the empty surroundings into the lenslets. We previously demonstrated SPOT for fluorescence imaging, in which only the fluorescent part of the sample contributes to the image. Figures 6(b) and 6(e) show that SPOT, and other light field microscopy, can underestimate the absorption in transmission imaging, when it is used without a carefully designed illumination system. Figure 6(c) shows the raw image acquired with the illumination pinhole. Although the aperture stop in the imaging beam path was completely open, the ghost images of nearby beads did not appear, which is due to the selective illumination enabled by the pinhole. Figure 6(f) shows that, after the background normalization, the projection images clearly show the bead regions with proper amount of absorption.

Starting from the scalar wave equation, we derived Eq. (7) by introducing a couple of approximations. The most notable one is the projection approximation, which assumes that the light propagates along the direction of incident beam throughout the entire sample. The use of projection approximation may be justified by the low ef-

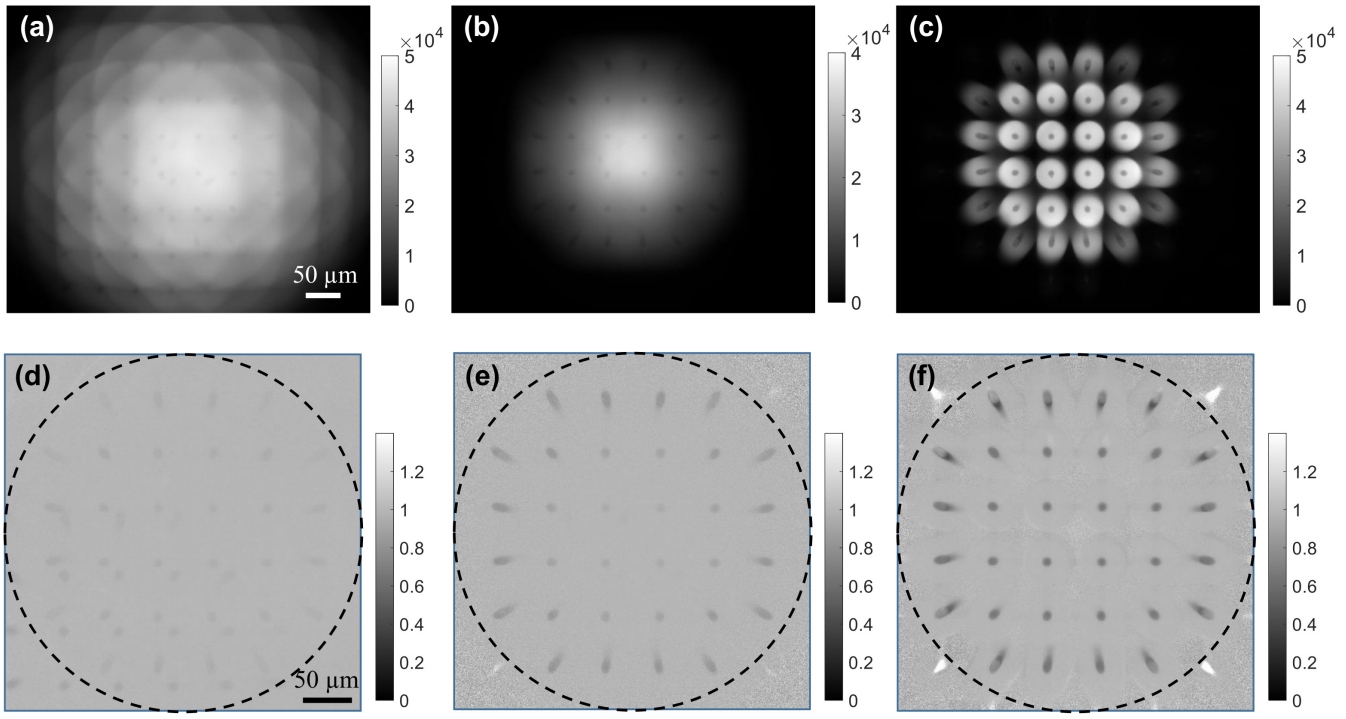

FIG. 6. Example raw images showing the effect of illumination pinhole. (a) An image of a blue-dyed polystyrene bead acquired without the illumination pinhole and the aperture stop, (b) an image of the same bead without the illumination pinhole but with the aperture stop, and (c) an image of the same bead with the illumination pinhole but without the aperture stop. Figures (d) through (f) are the normalized images of (a) through (c) using the corresponding background images.

fective NA of lenslets[28]. In deriving Eq. (7), we further approximated $1/w$, the multiplication factor in Eq. (2b), as $1/w_0$. The effect of the change is nonlinear and problem dependent. To estimate the relative magnitude of the error introduced by the approximation, we performed a simulation. Figure 7 shows simulated projection images of an absorbing spherical bead for the incidence angle of 42.1°. Figure 7(a) was calculated using Eq. (2b), and Fig. 7(b) was calculated after replacing $1/w$ with $1/w_0$ in Eq. (2b). Figure 7(c) shows the difference between Figs. 7(a) and 7(b) after the normalization with the intensity in Fig. 7(a). Figure 7(d) shows the profiles along the dotted lines in Figs. 7(a) and 7(c). The error introduced by the approximation is less than 2% throughout the entire region of simulated projection image.

Previously we demonstrated angular multiplexing of illumination beams for 3D snapshot imaging of refractive index map[28]. The technique called Snapshot holographic optical tomography (SHOT) uses an MLA to generate a multitude of collimated beams, each of which propagates through the sample along a different angle. The image generated by each beam can be interpreted as the projection of the refractive index map along the beam propagation direction. The so-called projection images overlap each other at the image plane, which is conjugate to the sample plane and where the camera is typically located. To separately record the projection images, we placed the camera at a defocused plane. By recording both the amplitude and phase images, instead of only the intensity, we can numerically propagate the projection images recorded at the defocused plane to the image plane, where the images are sharpest. Applying a tomographic reconstruction algorithm, the 3D refractive index map can be obtained from the projection images. In theory, the method can be used to provide the absorption coefficient as well as refractive index. However, the use of defocusing inevitably induces energy loss in each beam or information loss in each image, which may affect the accuracy of absorption measurement. Additional constraints may help to restore the missing information and allow for accurate measurement of absorption as well as phase[29].

Snapshot volumetric imaging techniques sacrifice the imaging resolution to obtain the depth information, which is completely missing in 2D imaging. This trade off can be justified when a series of volumetric images needs be acquired at high temporal resolution as in the monitoring of neuronal activity in a whole zebrafish brain[12]. Using a conventional 3D imaging method that relies on a scanning mechanism, it is not possible to monitor the entire volume at the required temporal resolution. Snapshot volumetric imaging will make it possible to obtain the 4D (3D space + 1D spectrum) data cube, or the chemical fingerprint at every voxel within the 3D vol-

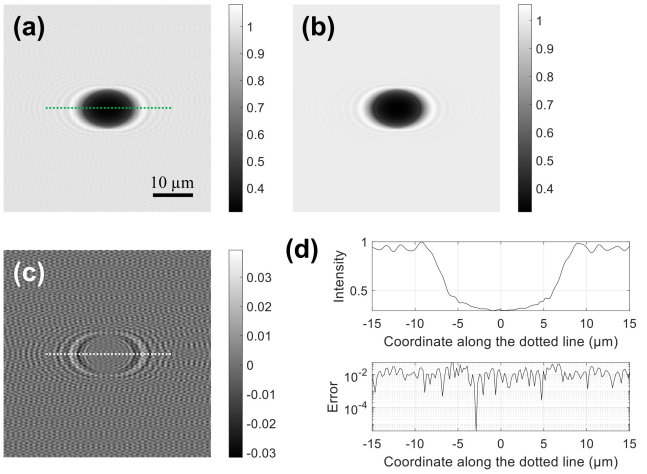

FIG. 7. Numerical simulation of projected images. (a) A projection image of an absorbing spherical bead simulated for the incident angle of 42.1°. (b) The same image generated using the approximation in Eq. (7). (c) The difference between (a) and (b). (d) The profiles along the dotted line in (a) and (c). The error was obtained by normalizing the difference shown in (c) with the value in (a).

ume, at unprecedented speed[3]. It will also enable us to record the 3D images of samples continuously moving at high speed as in 3D imaging flow cytometry[30]. In contrast to fluorescence imaging, which often operates in a photon-starved condition, absorption imaging has sufficient amount of light or signal available. Using a camera equipped with internal memory, the imaging throughput is only limited by the camera frame rate, although the number of images that can be acquired in a single experiment is limited by the memory size. With a camera that supports streaming to a hard disk, the imaging throughput is limited by the data download speed. Using the MLA as a tube lens, each projection image recorded with the developed system has the characteristics similar to those of a conventional bright-field image. The image contrast is the total amount of attenuation, which depends on both the attenuation coefficient and the thickness of the sample. The detection limit is ultimately determined by the dynamic range of the camera.

ACKNOWLEDGMENTS

This research was funded by the Research Growth Initiative of the University of Wisconsin-Milwaukee, the National Science Foundation (1808331), and the National Institute of General Medical Sciences of the National Institutes of Health (R21GM135848). Any opinions, findings, and conclusions or recommendations expressed in this material are those of the author and do not necessarily reflect the views of the National Institutes of Health.

[1] C. Sheppard, Depth of field in optical microscopy, J. Microsc. **149**, 73 (1988).
[2] J. G. McNally, T. Karpova, J. Cooper, and J. A. Conchello, Three-dimensional imaging by deconvolution microscopy, Methods **19**, 373 (1999).
[3] M. J. Nasse, M. J. Walsh, E. C. Mattson, R. Reininger, A. Kajdacsy-Balla, V. Macias, R. Bhargava, and C. J. Hirschmugl, High-resolution fourier-transform infrared chemical imaging with multiple synchrotron beams, Nat. Methods **8**, 413 (2011).
[4] A. C. Kak and M. Slaney, *Principles of Computerized Tomographic Imaging*, Vol. 33 (IEEE Press, New York, 1988).
[5] L. Gao and L. V. Wang, A review of snapshot multidimensional optical imaging: measuring photon tags in parallel, Phys. Rep. **616**, 1 (2016).
[6] A. Sinha, G. Barbastathis, W. Liu, and D. Psaltis, Imaging using volume holograms, Opt. Eng. **43**, 1959 (2004).
[7] P. M. Blanchard and A. H. Greenaway, Simultaneous multiplane imaging with a distorted diffraction grating, Appl. Opt. **38**, 6692 (1999).
[8] C. Maurer, S. Khan, S. Fassl, S. Bernet, and M. Ritsch-Marte, Depth of field multiplexing in microscopy, Opt. Express **18**, 3023 (2010).
[9] J. Yu, C. Zhou, W. Jia, J. Ma, A. Hu, J. Wu, and S. Wang, Distorted dammann grating, Opt. Lett. **38**, 474 (2013).
[10] M. Levoy, R. Ng, A. Adams, M. Footer, and M. Horowitz, Light field microscopy, ACM Trans. Graph. **25**, 924 (2006).
[11] A. Llavador, J. Sola-Pikabea, G. Saavedra, B. Javidi, and M. Martínez-Corral, Resolution improvements in integral microscopy with fourier plane recording, Opt. Express **24**, 20792 (2016).
[12] L. Cong, Z. Wang, Y. Chai, W. Hang, C. Shang, W. Yang, L. Bai, J. Du, K. Wang, and Q. Wen, Rapid whole brain imaging of neural activity in freely behaving larval zebrafish (danio rerio), Elife **6**, e28158 (2017).
[13] G. Scrofani, J. Sola-Pikabea, A. Llavador, E. Sanchez-Ortiga, J. Barreiro, G. Saavedra, J. Garcia-Sucerquia, and M. Martínez-Corral, Fimic: design for ultimate 3d-integral microscopy of in-vivo biological samples, Biomed. Opt. Express **9**, 335 (2018).
[14] C. Guo, W. Liu, X. Hua, H. Li, and S. Jia, Fourier light-field microscopy, Opt. Express **27**, 25573 (2019).
[15] Y. Sung, Snapshot projection optical tomography, Phys. Rev. Appl. **13**, 054048 (2020).
[16] J. W. Goodman, *Introduction to Fourier optics* (Roberts & Company Publishers, Greenwood Village, 2004).
[17] M. Born and E. Wolf, *Principles of Optics* (Cambridge University Press, Cambridge, 2019).
[18] E. Wolf, Three-dimensional structure determination of semi-transparent objects from holographic data, Opt. Commun. **1**, 153 (1969).
[19] A. Devaney, Inverse-scattering theory within the rytov approximation, Opt. Lett. **6**, 374 (1981).
[20] Y. Sung, W. Choi, C. Fang-Yen, K. Badizadegan, R. R. Dasari, and M. S. Feld, Optical diffraction tomography

for high resolution live cell imaging, Opt. Express **17**, 266 (2009).
[21] D. F. Swinehart, The beer-lambert law, J. Chem. Educ. **39**, 333 (1962).
[22] W. H. Richardson, Bayesian-based iterative method of image restoration, J. Opt. Soc. Am. **62**, 55 (1972).
[23] L. B. Lucy, An iterative technique for the rectification of observed distributions, Astron. J. **79**, 745 (1974).
[24] Y. Sung and R. R. Dasari, Deterministic regularization of three-dimensional optical diffraction tomography, J. Opt. Soc. Am. A **28**, 1554 (2011).
[25] Y. Sung, W. Choi, N. Lue, R. R. Dasari, and Z. Yaqoob, Stain-free quantification of chromosomes in live cells using regularized tomographic phase microscopy, PLoS One **7**, e49502 (2012).
[26] Y. Sung, Spectroscopic microtomography in the visible wavelength range, Phys. Rev. Appl. **10**, 054041 (2018).
[27] G. A. Tsihrintzis and A. J. Devaney, Higher order (nonlinear) diffraction tomography: Inversion of the rytov series, IEEE Trans. Inf. Theory **46**, 1748 (2000).
[28] Y. Sung, Snapshot holographic optical tomography, Phys. Rev. Appl. **11**, 014039 (2019).
[29] V. Katkovnik, Phase retrieval from noisy data based on sparse approximation of object phase and amplitude, arXiv preprint arXiv:1709.01071 (2017).
[30] Y. Sung, N. Lue, B. Hamza, J. Martel, D. Irimia, R. R. Dasari, W. Choi, Z. Yaqoob, and P. So, Three-dimensional holographic refractive-index measurement of continuously flowing cells in a microfluidic channel, Phys. Rev. Appl. **1**, 014002 (2014).